

HIGHLY IONIZED Fe–K ABSORPTION LINE FROM CYGNUS X-1 IN THE HIGH/SOFT STATE OBSERVED WITH *SUZAKU*

S. YAMADA¹, S. TORII², S. MINESHIGE³, Y. UEDA⁴, A. KUBOTA⁵, P. GANDHI⁶, C. DONE⁷,
H. NODA², A. YOSHIKAWA¹, AND K. MAKISHIMA^{1,2}

¹ Cosmic Radiation Laboratory, Institute of Physical and Chemical Research (RIKEN), Wako, Saitama 351-0198, Japan

² Department of Physics, University of Tokyo, 7-3-1 Hongo, Bunkyo-ku, Tokyo 113-0033, Japan

³ Department of Astronomy, Kyoto University, Kitashirakawa-Oiwake-cho, Sakyo-ku, Kyoto 606-8502, Japan

⁴ Department of Physics, Kyoto University, Kitashirakawa-Oiwake-cho, Sakyo-ku, Kyoto 606-8502, Japan

⁵ Department of Electronic Information Systems, Shibaura Institute of Technology, 307 Fukasaku, Minuma-ku, Saitama-shi, Saitama 337-8570, Japan

⁶ Institute of Space and Astronautical Science, JAXA, 3-1-1 Yoshinodai, Sagamiharas, 229-8510 Kanagawa, Japan

⁷ Department of Physics, Durham University, South Road, Durham DH1 3LE, UK

Received 2012 December 20; accepted 2013 February 23; published 2013 April 8

ABSTRACT

We present observations of a transient He-like Fe $K\alpha$ absorption line in *Suzaku* observations of the black hole binary Cygnus X-1 on 2011 October 5 near superior conjunction during the high/soft state, which enable us to map the full evolution from the start to the end of the episodic accretion phenomena or dips for the first time. We model the X-ray spectra during the event and trace their evolution. The absorption line is rather weak in the first half of the observation, but instantly deepens for ~ 10 ks, and weakens thereafter. The overall change in equivalent width is a factor of ~ 3 , peaking at an orbital phase of ~ 0.08 . This is evidence that the companion stellar wind feeding the black hole is clumpy. By analyzing the line with a Voigt profile, it is found to be consistent with a slightly redshifted Fe xxv transition, or possibly a mixture of several species less ionized than Fe xxv. The data may be explained by a clump located at a distance of $\sim 10^{10-12}$ cm with a density of $\sim 10^{(-13)-(-11)}$ g cm⁻³, which accretes onto and/or transits the line of sight to the black hole, causing an instant decrease in the observed degree of ionization and/or an increase in density of the accreting matter. Continued monitoring for individual events with future X-ray calorimeter missions such as *ASTRO-H* and *AXSIO* will allow us to map out the accretion environment in detail and how it changes between the various accretion states.

Key words: stars: individual (Cyg X-1) – X-rays: binaries

Online-only material: color figures

1. INTRODUCTION

Mass accretion onto a black hole binary (BHB) produces energetic astrophysical phenomena. BHBs are largely classified into two distinct states: high/soft and low/hard (e.g., Remillard & McClintock 2006). Mass accretion is believed to be provided by the stellar wind from the companion star for high-mass X-ray binaries, while it is caused by Roche lobe overflow for low-mass X-ray binaries. X-ray absorption features have been observed from both systems, and have been interpreted as the absorption by the disk wind, the stellar wind, or the hot spot on the disk. Such an absorption feature can be crucial to probe the global structure of the accretion flow that is presumably related to the differences between the two states.

Cyg X-1 is a famous BHB and belongs to one of the high-mass X-ray binaries (Oda et al. 1971; Tananbaum et al. 1972). It has an O9.7 Iab supergiant, HD 226868 (Caballero-Nieves et al. 2009). The distance, mass, and inclination are $D = 1.86_{-0.11}^{+0.12}$ kpc (Reid et al. 2011; Xiang et al. 2011), $M = 14.8 \pm 1.0 M_{\odot}$, and $i = 27^{\circ}.1 \pm 0^{\circ}.8$ (Orosz et al. 2011), respectively. The orbital period is 5.599829 days (Brocksopp et al. 1999). Since HDE 226868 almost fills its Roche lobe in Cyg X-1 (Gies & Bolton 1986), the stellar wind is not spherically symmetric but strongly enhanced toward the BH (“focused wind”; Friend & Castor 1982).

The stellar wind causes episodes of increased absorption, or “dips,” which are seen as a decrease in soft X-ray flux (e.g., Pravdo et al. 1980; Kitamoto et al. 1984) mostly near the superior conjunction of the BH (when the observer, the companion star,

and the BH are aligned in this order). In long-term continuous monitoring with *RXTE*, these dips have rarely been seen in the high/soft state in contrast to the frequent occurrence in the low/hard state (Wen et al. 1999). Detailed studies of the absorption feature have been realized with *Chandra*/HETG observations of Cyg X-1 in several orbital phases ϕ_{orb} and states; e.g., $\phi_{\text{orb}} \approx 0.74$ (Schulz et al. 2002) and $\phi_{\text{orb}} \approx 0$ (Hanke et al. 2009) in the low/hard state, $\phi_{\text{orb}} \approx 0.77$ (Miller et al. 2005) in the intermediate state, and $\phi_{\text{orb}} \approx 0.88$ (Chang & Cui 2007) and $\phi_{\text{orb}} \approx 0$ (Feng et al. 2003) in the high/soft state. Despite these observations, the differences in absorbing matter between the low/hard state and the high/soft state are poorly understood, probably due to fewer observations in the high/soft state.

Cyg X-1 usually stays in the low/hard state, though it recently has changed into the high/soft state since the middle of 2010. Thus, we observed Cyg X-1 twice with *Suzaku* (Mitsuda et al. 2007) in the high/soft state and found clear absorption features at around the Fe–K band in the latter observation performed at $\phi_{\text{orb}} \approx 0.05$. In this Letter, we report the detection of the He-like Fe $K\alpha$ absorption line with *Suzaku* and its full evolution. Unless otherwise stated, errors refer to 90% confidence limits.

2. OBSERVATION AND ANALYSIS

2.1. Observation

Cyg X-1 was observed with *Suzaku* on 2010 December 16 (Obs. 1; ObsID = 905006010) and 2011 October 5 (Obs. 2; ObsID = 406013010). The corresponding orbital phases are $\phi_{\text{orb}} \approx 0.64\text{--}0.80$ for Obs. 1 and $\phi_{\text{orb}} \approx 0.98\text{--}0.13$ for Obs. 2,

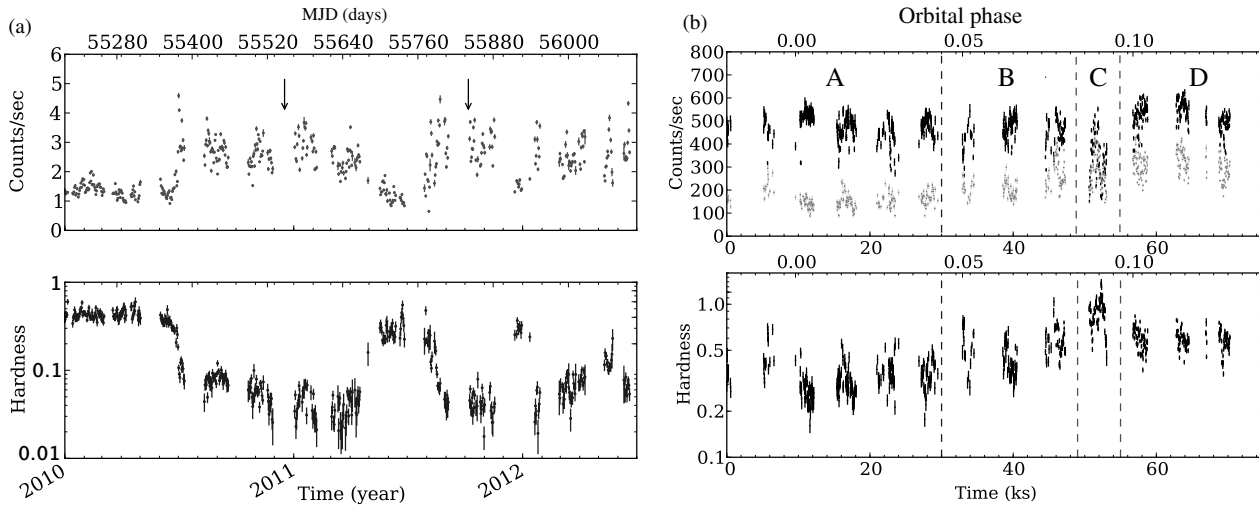


Figure 1. (a) 2–20 keV Cyg X-1 light curve of MAXI GSC and the hardness of 10–20 keV to 2–4 keV. The two arrows indicate Obs. 1 and Obs. 2, respectively. (b) The 0.5–1.5 keV (black) and 3–10 keV (gray) light curves and the hardness of 3–10 keV to 0.5–1.5 keV, taken from *Suzaku* Obs. 2 with time bin size of 32 s. The orbital phases are plotted on the top. Phases A, B, C, and D are indicated in the plot.

assuming that an epoch of the superior conjunction of the BH is MJD41874.207 based on Brocksopp et al. (1999). XIS employed the 1/4 window option and a burst mode of 0.5 s (Koyama et al. 2007; see Serlemitsos et al. 2007 on the X-ray mirror). HXD-PIN and HXD-GSO were operated in standard mode (Takahashi et al. 2007; Kokubun et al. 2007; Yamada et al. 2011).

The long-term light curve and hardness of Cyg X-1 taken from the archival data of the MAXI Gas Slit Camera (MAXI: Matsuoka et al. 2009; GSC: Sugizaki et al. 2011) are shown in Figure 1(a). Although Cyg X-1 was believed to stay mostly in the low/hard state, it has been in the high/soft state (the hardness ratios $\lesssim 0.2$) over the last two years. The first and second observations were performed during the high/soft state as indicated in Figure 1(a).

2.2. Data Reduction

The data processing and reduction were performed by using the *Suzaku* pipeline processing version 2.7.16.30. The XIS data are reprocessed by running `xispi` with the latest gain calibration file of `ae_xi?_makepi_20120527.fits`. Events were discarded if they were acquired in the South Atlantic Anomaly, or in regions of low cutoff rigidity (≤ 6 GV for both XIS and HXD), or with low Earth elevation angles. The exposures of the XIS and HXD data in Obs. 1 and Obs. 2 were 2.9 ks and 28.4 ks, and 3.8 ks and 26.3 ks, respectively. The reason that the exposure of XIS is shorter than that of HXD is due to utilizing the burst option (live time fraction of 25%) and discarding the period in which the telemetry of XIS is saturated. We subtracted the modeled non-X-ray backgrounds (Fukazawa et al. 2009) from the HXD spectra, but did not subtract the background from the XIS spectra because the background is less than $\sim 0.1\%$ in any energy bands below ~ 10 keV. We used a standard set of the response files and the auxiliary files; i.e., ones generated by running `xismfgen` and `xissimarfgen` (Ishisaki et al. 2007) and provided as the CALDB files for *Suzaku* users.

We estimated pileup effects on XIS and excised the image core within a pileup fraction larger than 3% ($\sim 1'$) according to the empirical criteria (Yamada et al. 2012). Since the pileup effect distorts the continuum but leaves the narrow line features rather untouched, we used a circular region of XIS for Obs. 2 to

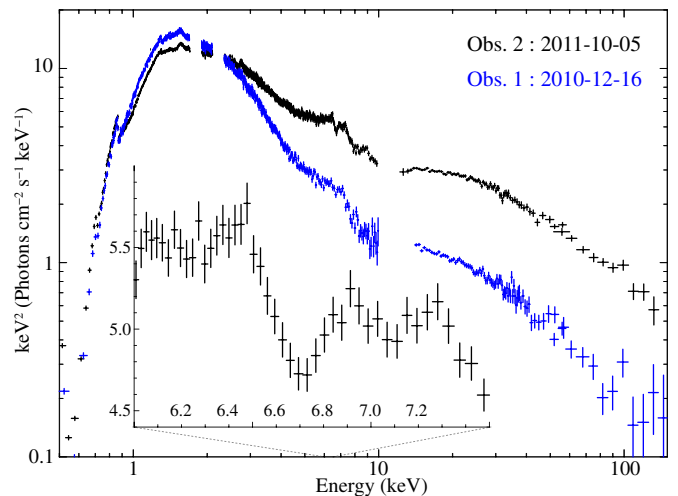


Figure 2. Cyg X-1 wide-band spectra in the νF_ν form in Obs. 1 (blue) and Obs. 2 (black) taken from *Suzaku*/XIS, PIN, and GSO. The 6–7.5 keV band of Obs. 2 is inserted in the bottom left panel. The 1.7–1.9 keV and 2.1–2.3 keV bands are discarded due to instrumental uncertainties on Si and Au edges.

(A color version of this figure is available in the online journal.)

maximize photon statistics, together with an additional auxiliary file to correct for continuum distortion caused by pileup. Comparing the XIS spectrum, including the image core with the one excluding the core when those are used with the auxiliary files, we confirmed that its difference is less than $\sim 2\%$, and thus we adopted a systematic uncertainty of 2% when performing spectral fitting.

2.3. Wide-band Spectra

Figure 2 shows wide-band spectra taken from Obs. 1 and Obs. 2. The spectrum of the former shows a prominent disk emission below ~ 10 keV and a power-law tail with reflected emission, which are typically seen in the high/soft state. On the other hand, the spectrum of the latter shows not only more enhanced power-law emission but also absorption features at ~ 6.7 keV and ~ 7.1 keV as seen in the subset in Figure 2.

We perform in this Letter an analysis of the XIS0 data in Obs. 2 to concentrate on the absorption features. Note that such

an absorption feature can be seen in the XIS3 and XIS1 spectra, but XIS3 is operated in timing mode, and XIS1 is a backside illuminated CCD, which make it hard to treat all the XIS data in a comprehensive manner, especially under conditions being affected by pileup. More detailed analysis on the wide-band spectra will be described in a subsequent paper.

2.4. Light Curves

Figure 1(b) shows the light curves of XIS0 in Obs. 2. The 0.5–1.5 keV count rate is approximately constant at ~ 500 counts s^{-1} , though it significantly decreases to ~ 300 counts s^{-1} at $\phi_{\text{orb}} \simeq 0.08$. Meanwhile, the 3–10 keV count rate is rather monotonically increasing from ~ 100 counts s^{-1} to ~ 300 counts s^{-1} over the entire observation and does not show a significant decrease at $\phi_{\text{orb}} \simeq 0.08$.

The hardness ratio, as shown in the bottom of Figure 1(b), has gradually increased to ~ 1.0 toward $\phi_{\text{orb}} \approx 0.08$ and afterward decreases to ~ 0.5 . This rapid change in hardness around $\phi_{\text{orb}} \approx 0.08$ is probably caused by dips, while the gradual spectral changes over the entire observation seem intrinsic to the central source. To study more concretely the spectral evolution depending on the luminosity and ϕ_{orb} , we define Phases A, B, C, and D, as shown in Figure 1(b), to examine each spectrum in detail. The dip marginally appears in Phase A and Phase B, and certainly occurs in Phase C, and gradually disappears in Phase D.

3. SPECTRAL ANALYSIS AND RESULTS

3.1. Spectral Features in Each Phase

Figure 3(a) shows the unfolded spectra of XIS0 taken from the four phases. The spectrum becomes harder as the source becomes brighter by a factor of ~ 3 . The deepest absorption feature at ~ 6.7 keV can be seen most clearly in Phase C. In contrast, the absorption feature in Phase A is shallower than the others. The overall shape of the spectra is not straight even in such a narrowband, which is caused by a broad Fe–K emission line, and Fe edges (Dotani et al. 1997), and concave continua probably consisting of a blend of disk emission, non-thermal emission, and associated reflection. The similar trend is reported in a previous study (e.g., Feng et al. 2003).

Since our aim is to quantify absorption lines and temporal variations, we employed conventional models implemented in XSPEC as an underlying continuum to fit the spectra, i.e., `tbabs*edge*(diskbb+power)`, where `tbabs` is interstellar absorption (Wilms et al. 2000) and `diskbb` is disk blackbody emission (Mitsuda et al. 1984; Makishima et al. 1986). We first tried to approximate an absorption or emission line with a Gaussian because the statistical errors are not small enough to determine the precise line profile. To make spectral changes more clear, we took the ratios of the four spectra to the model adjusted to fit the spectrum of Phase A. By looking at the ratios as illustrated in Figure 3(b), we find it more obvious that the spectrum hardens as the flux increases and the absorption is deepest in Phase C.

3.2. Quantification of the Absorption Line

We then tried to quantify the four phase-sliced spectra and the entire spectra (Phase All). We first checked whether the two absorption lines at ~ 6.7 and ~ 7.0 keV are statistically significant by fitting the five spectra over the narrow energy range around these lines with `gauss+power`. The former is

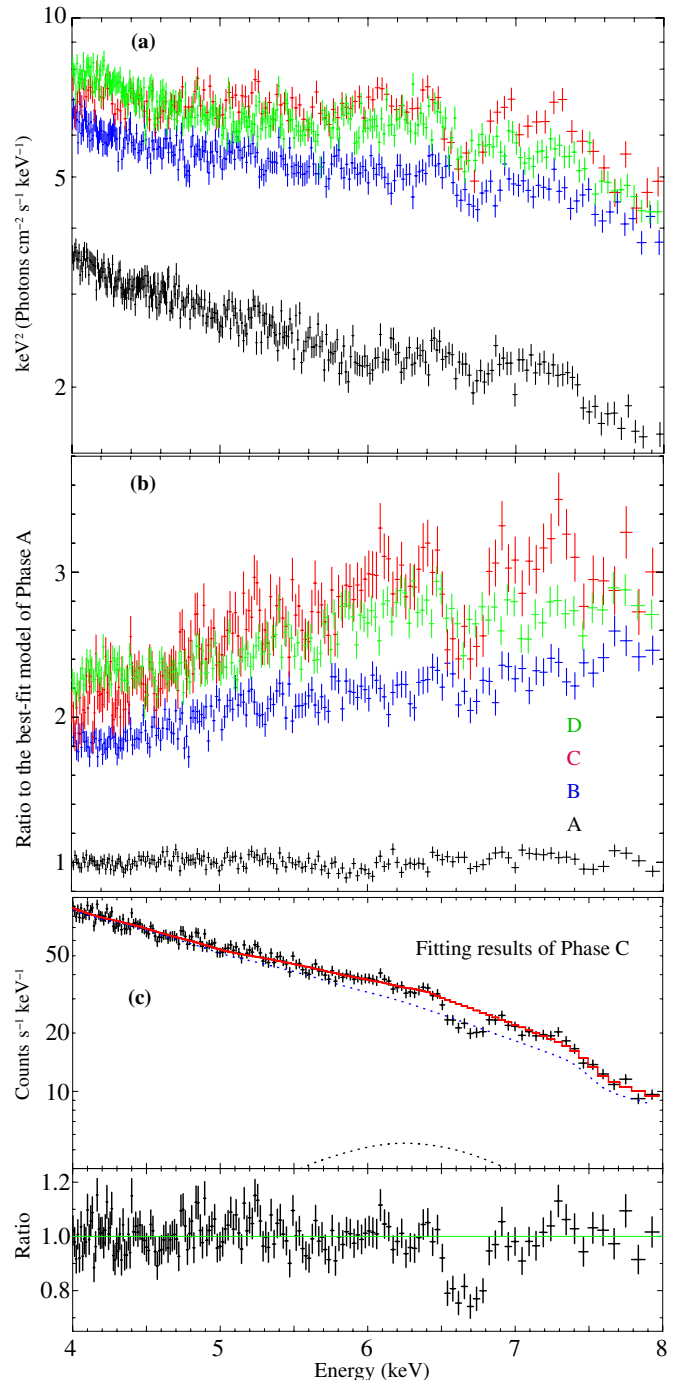


Figure 3. (a) Cyg X-1 $\nu F\nu$ spectra of XIS0 for the four phases. (b) The spectral ratios of the four spectra to the best-fit model of Phase A. The colors of the labels indicate each phase. (c) The best-fit model shown in red and the detector-response-convolved spectrum of Phase C, and the spectral ratio to the model except for the absorption line.

(A color version of this figure is available in the online journal.)

found to be significant with a higher than 3σ level, but the latter is rather marginal with a $\sim 1\sigma$ level for all spectra.

Then the fits over 4–8 keV are performed with the baseline continuum, two narrow negative Gaussians as the absorption lines at ~ 6.7 keV and ~ 7.0 keV, and a broad and narrow positive Gaussian as the emission lines at ~ 6.4 keV, i.e., `tbabs*edge*(diskbb+power+gauss($\times 4$))`. The central energy E_c and the width of the absorption line for the ~ 6.7 keV line are fixed at 6.698 keV for He-like Fe xxv and 0.1 eV,

Table 1
Best-fit Parameters of the XIS0 Spectrum for Each Phase and Entire Observation

Parameters	A	B	C	D	All
He-like Fe xxv absorption line					
E_c (keV)	6.698(fix)	6.698(fix)	$6.614^{+0.034}_{-0.085}$	6.698(fix)	$6.664^{+0.025}_{-0.013}$
σ (eV)	0.1 (fix)	0.1 (fix)	$90.5^{+100.1}_{-51.5}$	0.1 (fix)	$32.8^{+32.7}_{-32.8}$
Norm. (10^{-3} photons cm^{-2} s^{-1})	$0.60^{+0.55}_{-0.40}$	$2.31^{+0.89}_{-0.86}$	$10.3^{+2.24}_{-1.56}$	$3.40^{+1.01}_{-1.00}$	$2.94^{+0.49}_{-0.35}$
EW (eV)	$11.8^{+10.8}_{-7.9}$	$20.4^{+7.9}_{-7.6}$	$66.0^{+14.4}_{-10.0}$	$24.6^{+7.3}_{-7.2}$	$24.3^{+4.1}_{-2.9}$
H-like Fe xxvi absorption line ^a					
Norm. (10^{-3} photons cm^{-2} s^{-1})	$0_{-0.13}$	$0.02^{+0.01}_{-0.02}$	$0.58^{+1.71}_{-0.58}$	$3.40^{+0.98}_{-0.98}$	$0.50^{+0.50}_{-0.50}$
EW (eV)	$0_{-0.03}$	$0.2^{+1.0}_{-0.2}$	$4.5^{+13.3}_{-4.5}$	$9.3^{+2.7}_{-2.7}$	$4.8^{+4.8}_{-4.8}$
Neutral Fe K α narrow emission line ^b					
Norm. (10^{-3} photons cm^{-2} s^{-1})	$0.4^{+0.4}_{-0.4}$	$1.2^{+0.9}_{-0.9}$	$2.6^{+2.2}_{-1.9}$	$1.0^{+1.1}_{-1.0}$	$0.9^{+0.4}_{-0.5}$
Neutral Fe K α broad line ^b					
Norm. (10^{-2} photons cm^{-2} s^{-1})	$1.20^{+0.22}_{-1.20}$	$0.23^{+0.25}_{-2.54}$	$1.12^{+0.56}_{-1.88}$	$8.95^{+2.83}_{-2.60}$	$5.12^{+0.22}_{-0.20}$
Continuum ^c					
τ^d	$0.21^{+0.04}_{-0.04}$	$0.16^{+0.08}_{-0.06}$	$0.33^{+0.05}_{-0.05}$	$0.06^{+0.07}_{-0.06}$	$0.12^{+0.02}_{-0.02}$
N_{dbb}^e ($10^5 R_{\text{in}}^2 D_{10}^{-2} \cos \theta$)	$1.66^{+0.18}_{-0.21}$	$1.79^{+0.96}_{-0.60}$	$0.72^{+0.92}_{-0.72}$	$2.33^{+1.12}_{-1.44}$	$1.47^{+0.15}_{-0.16}$
Γ	$2.67^{+0.06}_{-0.12}$	$2.36^{+0.15}_{-0.14}$	$2.16^{+0.17}_{-0.16}$	$2.93^{+0.27}_{-0.24}$	$2.71^{+0.02}_{-0.02}$
N_{pi} (photons keV^{-1} cm^{-2} s^{-1} at 1 keV)	$7.96^{+0.88}_{-1.64}$	$9.88^{+4.23}_{-1.30}$	$8.92^{+4.30}_{-1.29}$	$27.5^{+15.2}_{-8.7}$	$17.5^{+2.51}_{-0.10}$
χ^2_{ν} (dof)	1.07(160)	0.98(160)	1.01(158)	1.12(160)	1.18(158)
Kabs ^f [$b = 100 \text{ km s}^{-1}$]					
z (10^{-3})	0. (fix)	0. (fix)	$9.4^{+2.5}_{-3.6}$	0. (fix)	$3.0^{+2.5}_{-2.7}$
$N_{\text{Fe xxv}}$ (10^{19} cm^{-2})	$0.07^{+0.24}_{-0.06}$	$0.29^{+0.54}_{-0.23}$	$6.54^{+3.28}_{-2.65}$	$0.55^{+0.62}_{-0.37}$	$0.59^{+0.34}_{-0.25}$
χ^2_{ν} (dof)	1.07(160)	0.98(160)	1.02(159)	1.11(160)	1.18(159)

Notes.

^a The value of E_c and the width is fixed at 6.966 keV and 0.1 eV, respectively.

^b The value of E_c is fixed at 6.4 keV, while the width is fixed at 0.1 eV for the narrow line and 1.0 keV for the broad line.

^c The neutral column density is fixed at $7.0 \times 10^{21} \text{ cm}^{-2}$.

^d The energy of the edge is fixed at 7.5 keV.

^e The temperature of the disk is fixed at 0.4 keV. R_{in} and D_{10} are inner radius and the distance in units of 10 kpc.

^f A Kabs model for He-like Fe K α is used in place of a negative Gaussian at ~ 6.7 keV.

respectively. They are left free for Phase C and Phase All, while being kept fixed for the others. The value of E_c and the width for the ~ 7.0 keV line are fixed at 6.966 keV for H-like Fe xxvi and 0.1 eV, respectively. They were not freed due to poor photon statistics. The obtained fitting results are summarized in Table 1. Due to the limited energy range, some of the parameters of the continua are left fixed as shown in the notes of Table 1. As a result, all fits became statistically acceptable.

The best-fit model and the spectra of Phase C are presented in Figure 3(c) as an example, as well as the spectral ratio to the model from which the absorption lines are purposely removed just to visualize the absorption feature. The absorption line of He-like Fe xxv is evidently detected, while that of H-like Fe xxvi can be barely seen. The values of E_c are slightly lower than He-like Fe xxv (6698 eV at rest). The difference is larger than a systematic uncertainty ~ 10 eV for XIS operated with a window option,⁸ suggesting the possibilities of the contribution from lower ionized species than Fe xxv and/or redshifted absorption lines. The resultant values of an equivalent width (EW) are plotted in Figure 4. As expected, the absorption line is gradually deepening from EW ~ 10 eV to EW ~ 60 eV toward Phase C, and then to EW ~ 20 eV.

For a detailed analysis of the absorption line, we used a Voigt profile implemented in XSPEC as a local model of Kabs (Ueda

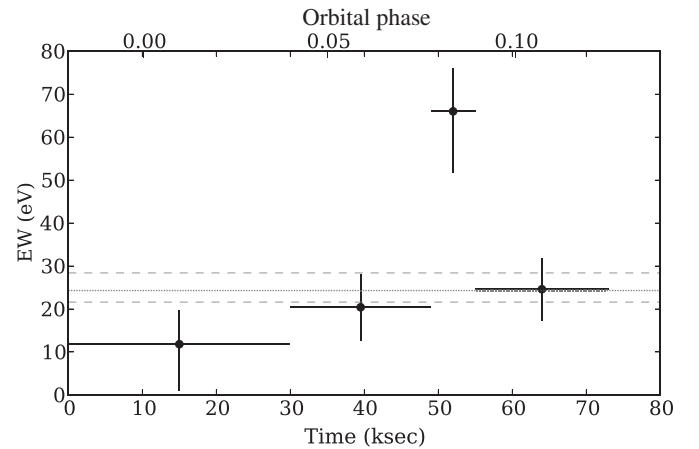


Figure 4. Fitting results of EW for the He-like Fe K α absorption line taken from Phase A to Phase D. The mean value and the upper and lower errors taken from Phase All are overlaid in dotted and dashed lines, respectively.

et al. 2004; see also Kubota et al. 2007) which has three fitting parameters of the ion column density N_{ion} , the radial velocity dispersion b , and a redshift for bulk motion z . Since the value of b cannot be well constrained by the line profile, we fixed b at 100 km s^{-1} . The value of z is left free only for Phase C and Phase All. The resultant parameters are summarized in Table 1. When we changed b to 300 km s^{-1} , the values of $N_{\text{Fe xxv}}$ and

⁸ http://heasarc.gsfc.nasa.gov/docs/heasarc/caldb/suzaku/docs/xis/20111228_MakepiUpdate_win14GainTable.pdf

z are obtained as $1.70_{-1.05}^{+2.56} \times 10^{19} \text{ cm}^{-2}$ and $8.2_{-5.0}^{+3.3} \times 10^{-3}$ for Phase C, and $0.82_{-0.27}^{+0.41} \times 10^{19} \text{ cm}^{-2}$ and $3.5_{-2.6}^{+2.5} \times 10^{-3}$ for Phase All, respectively, which are slightly different from those in the case of $b = 100 \text{ km s}^{-1}$ as shown in Table 1. Thus, it is certain that the relative value of the column density increases toward Phase C. When we forced z to be fixed at 0 and added a negative narrow Gaussian, the fit became acceptable with χ_v^2 (dof) = 1.01(160), resulting in $E_c = 6539_{-44}^{+38} \text{ eV}$ and $EW = 33.5 \pm 10.7 \text{ eV}$. Therefore, the data also imply the presence of lower ionized species like Fe XXI.

4. DISCUSSION AND SUMMARY

We have obtained two *Suzaku* observations of Cyg X-1 in the high/soft state and found not only the He-like Fe $K\alpha$ absorption line but also studied its time evolution from $\phi_{\text{orb}} \sim 0.98$ to ~ 0.13 . Although the absorption line is detected with *Chandra*/HETG (Feng et al. 2003) during the high/soft state, it is more obviously detected with *Suzaku*/XIS so that we can map the full evolution from the start and the end of the dip event. The detection is clearly obtained at $\phi_{\text{orb}} \approx 0.08$, which may be slightly later than the *Chandra* observation at $\phi_{\text{orb}} \approx 0$. A H-like Fe $K\alpha$ absorption line appears to be detected, though it is not statistically significant.

By dividing the entire span of Obs. 2 into the four phases, we obtained the spectral evolution as a function of time (Figures 3(a) and (b)) and quantified their changes (Table 1). By quantifying the spectra with the conventional models, we found that the EW gradually increases from $\sim 10 \text{ eV}$ ($\phi_{\text{orb}} \approx 0.95$) to $\sim 60 \text{ eV}$ ($\phi_{\text{orb}} \approx 0.08$) and decreases to $\sim 20 \text{ eV}$ ($\phi_{\text{orb}} \approx 0.15$). In short, the He-like Fe $K\alpha$ absorption line increases in EW by a factor of ~ 3 for less than $\sim 10 \text{ ks}$, as shown in Figure 4. If absorption lines were driven by the continuous disk wind, they could be observed independently of the orbital period, e.g., the absorption lines are detected from GRO J1655–40 over the entire orbital period without any significant change (Yamaoka et al. 2001). Thus, the absorption lines that we found can be interpreted as an increase in absorbing matter from the stellar wind on that short timescale.

By fitting the absorption line with the Voigt profile by using the Kabs model, we evaluated $N_{\text{Fe XXV}}$ and z as summarized in Table 1. According to Hanke et al. (2009), the value of $N_{\text{Fe XXV}}$ in the low/hard state during the non-dipping period is estimated to be $1.5_{-0.4}^{+0.3} \times 10^{17} \text{ cm}^{-2}$, which is consistent with the lower limit that we derived from Phase A, $\sim 10^{17} \text{ cm}^{-2}$. The value of $N_{\text{Fe XXV}}$ in Phase C, $\sim 10^{19} \text{ cm}^{-2}$, corresponds to N_{H} of $\sim 2 \times 10^{23} \text{ cm}^{-2}$ when an abundance ratio of Fe to H is assumed to be 5×10^{-5} (Anders & Grevesse 1989). The redshift of $z = 9.4_{-3.6}^{+2.5} \times 10^{-3}$ obtained from Phase C corresponds to $2900_{-1200}^{+700} \text{ km s}^{-1}$ when we take it at its face value. The value grossly corresponds to a free fall velocity, $\sqrt{GM/r} \sim 4400 \text{ km s}^{-1}$, where G is the gravitational constant and the distance from the absorber to the source r is 10^{10} cm . Alternatively, we can assume that an absorbing blob rotating at a distance from the BH to the common center of mass, $\sim 1.7 \times 10^{12} \text{ cm}$ (Orosz et al. 2011), can traverse our line of sight for $3.4 \times 10^{11} \text{ cm}$ with a rotational velocity of $\sim 340 \text{ km s}^{-1}$ for a duration in Phase C of $\sim 10 \text{ ks}$. By putting together all the results, it can be interpreted that some patchy matter provided by the stellar wind, presumably located at $r \sim 10^{10-12} \text{ cm}$ with a hydrogen density of $\sim 10^{11-13} \text{ cm}^{-3}$ or $\sim 10^{(-13)-(-11)} \text{ g cm}^{-3}$, accretes onto and/or transits the BH, causing an instant decrease in the degree of ionization of the covering material and/or an increase in the density of

the accreting matter. Since several uncertainties could exist on the absolute energy scale of XIS and contamination from lower ionized species indistinguishable from Fe XXV, continued monitoring with future X-ray calorimeter missions such as *ASTRO-H/SXS* (Takahashi et al. 2010) and *AXSIO* (Bookbinder et al. 2012), will allow us to map out the accretion environment more precisely.

In the low/hard state, such a highly ionized Fe–K absorption line has rarely been detected though the dips occur more frequently than in the high/soft state. It is simply interpreted that the absorbing matter in the high/soft state has either lower density or higher ionization than in the low/hard state. However, the number of the photons in energies above $\sim 7 \text{ keV}$ in the low/hard state is more than that in the high/soft state. This implies that there could be some geometrical effects, such as an accretion stream and changes in the scale heights of the X-ray emitting coronae (Wen et al. 1999) or the precession of the accretion disk with an accretion bulge (Poutanen et al. 2008).

From Obs. 1 performed for $\phi_{\text{orb}} \approx 0.64\text{--}0.80$, we could not see any absorption features (Figure 2). Could the appearance of the absorption feature be related to the strength of the power-law emission or did we just find the absorption feature when the power-law emission is brighter by chance? More comprehensive observations for the dipping phenomena in different spectral states would be crucial to obtain the whole picture of the stellar wind and the accretion flow around the BH.

The authors express their thanks to the *Suzaku* team members. The research presented in this Letter has been funded by the Special Postdoctoral Researchers Program in RIKEN and JSPS KAKENHI grant No. 24740129. S.T. and H.N. are supported by a Grant-in-Aid for JSPS Fellows.

REFERENCES

- Anders, E., & Grevesse, N. 1989, *GeCoA*, **53**, 197
 Bookbinder, J. A., Smith, R. K., Bandler, S., et al. 2012, *Proc. SPIE*, **8443**, 17
 Brocksopp, C., Tarasov, A. E., Lyuty, V. M., & Roche, P. 1999, *A&A*, **343**, 861
 Caballero-Nieves, S. M., Gies, D. R., Bolton, C. T., et al. 2009, *ApJ*, **701**, 1895
 Chang, C., & Cui, W. 2007, *ApJ*, **663**, 1207
 Dotani, T., Inoue, H., Mitsuda, K., et al. 1997, *ApJL*, **485**, L87
 Feng, Y. X., Tennant, A. F., & Zhang, S. N. 2003, *ApJ*, **597**, 1017
 Friend, D. B., & Castor, J. I. 1982, *ApJ*, **261**, 293
 Fukazawa, Y., Mizuno, T., Watanabe, S., et al. 2009, *PASJ*, **61**, 17
 Gies, D. R., & Bolton, C. D. 1986, *ApJ*, **304**, 371
 Hanke, M., Wilms, J., Nowak, M. A., et al. 2009, *ApJ*, **630**, 330
 Ishisaki, Y., Maeda, Y., Fujimoto, R., et al. 2007, *PASJ*, **59**, 113
 Kitamoto, S., Miyamoto, S., Tanaka, Y., et al. 1984, *PASJ*, **36**, 731
 Kokubun, M., Makishima, K., Takahashi, T., et al. 2007, *PASJ*, **59**, S53
 Koyama, K., Tsunemi, H., Dotani, T., et al. 2007, *PASJ*, **59**, S23
 Kubota, et al. 2007, *PASJ*, **59**, 185
 Makishima, K., Maejima, Y., Mitsuda, K., et al. 1986, *ApJ*, **308**, 635
 Matsuoka, M., Kawasaki, K., Ueno, S., et al. 2009, *PASJ*, **61**, 999
 Miller, J. M., Wojdowski, P., Schulz, N. S., et al. 2005, *ApJ*, **620**, 398
 Mitsuda, K., Bautz, M., Inoue, H., et al. 2007, *PASJ*, **59**, 1
 Mitsuda, K., Inoue, H., Koyama, K., et al. 1984, *PASJ*, **36**, 741
 Oda, M., Gorenstein, P., Gursky, H., et al. 1971, *ApJL*, **166**, L1
 Orosz, J. A., McClintock, J. E., Aufdenberg, J. P., et al. 2011, *ApJ*, **742**, 84
 Poutanen, J., Zdziarski, A., & Ibragimov, A. 2008, *MNRAS*, **389**, 3, 1427
 Pravdo, S. H., White, N. E., Becker, R. H., et al. 1980, *ApJL*, **237**, L71
 Reid, M. J., McClintock, J. E., Narayan, R., et al. 2011, *ApJ*, **742**, 83
 Remillard, R. A., & McClintock, J. E. 2006, *ARA&A*, **44**, 49
 Schulz, N. S., Cui, W., Canizares, C. R., et al. 2002, *ApJ*, **565**, 1141
 Serlemitsos, P. J., Soong, Y., Chan, K.-W., et al. 2007, *PASJ*, **59**, 9
 Sugizaki, M., Mihara, T., Serino, M., et al. 2011, *PASJ*, **63**, 635
 Takahashi, H., Fukazawa, Y., Mizuno, T., et al. 2007, *PASJ*, **59**, 35
 Takahashi, T., Mitsuda, K., Kelley, R., et al. 2010, *Proc. SPIE*, **7732**, 77320Z

Tananbaum, H., Gursky, H., Kellogg, E., Giacconi, R., & Jones, C. 1972, [ApJL](#), [177](#), [L5](#)
Ueda, Y., Murakami, H., Yamaoka, K., Dotani, T., & Ebisawa, K. 2004, [ApJ](#), [609](#), [325](#)
Wen, L., Cui, W., Levine, A. M., & Bradt, H. V. 1999, [ApJ](#), [525](#), [968](#)

Wilms, J., Allen, A., & McCray, R. 2000, [ApJ](#), [542](#), [914](#)
Xiang, J., Lee, J. C., Nowak, M. A., & Wilms, J. 2011, [ApJ](#), [738](#), [78](#)
Yamada, S., Makishima, K., Nakazawa, K., et al. 2011, [PASJ](#), [63](#), [S645](#)
Yamada, S., Uchiyama, H., Dotani, T., et al. 2012, [PASJ](#), [64](#), [53](#)
Yamaoka, K., Ueda, Y., Inoue, H., & Nagase, F. 2001, [PASJ](#), [53](#), [179](#)